Acta Crystallographica Section D
Biological Crystallography
ISSN 0907-4449

Is radiation damage dependent on the dose rate used during macromolecular crystallography data collection?

Hanna-Kirsti S. Leiros,[a] Joanna Timmins,[a] Raimond B. G. Ravelli[b] and Seán M. McSweeney[a]*

[a]Macromolecular Crystallography Group, European Synchrotron Radiation Facility (ESRF), 6 Rue Jules Horowitz, 38043 Grenoble, France, and [b]European Molecular Biology Laboratory (EMBL) Grenoble Outstation, 6 Rue Jules Horowitz, 38042 Grenoble, France

Correspondence e-mail: mcsweeney@esrf.fr

Received 18 May 2005
Accepted 18 October 2005

PDB References: selenomethionine-substituted maltooligosyltrehalohydrolase, 2bxy, r2bxysf; 2bxz, r2bxzsf; 2by0, r2by0sf; 2by1, r2by1sf; 2by2, r2by2sf; 2by3, r2by3sf; bovine trypsin, 2by5, r2by5sf; 2by6, r2by6sf; 2by7, r2by7sf; 2by8, r2by8sf; 2by9, r2by9sf; 2bya, r2byasf.

This paper focuses on the radiation-damage effects when applying the same total X-ray dose to protein crystals at different dose rates. These experiments have been performed on both a selenomethionated protein and on bovine trypsin using dose rates that span nearly two orders of magnitude. The results show no clear dose-rate effect on the global indicators of radiation damage, but a small measurable dose-rate effect could be found when studying specific radiation damage. It is hypothesized that this observed dose-rate effect relates to differences in the steady-state free-radical concentration.

1. Introduction

The impact of radiation damage in macromolecular crystallography has become one of the major problems in the effective utilization of undulator radiation at third-generation synchrotron sources. Despite extensive investigation during recent years (Burmeister, 2000; Ravelli & McSweeney, 2000; Ravelli *et al.*, 2002; Weik *et al.*, 2000, 2002), the main way of coping with the problem is to reduce the exposure time as well as to attenuate and/or defocus the X-ray beam. Attenuation and defocusing affect the dose rate at which X-rays impinge on the sample.

There has been some controversy concerning the relative importance of absorbed dose and the rate at which the dose is applied. Sliz *et al.* (2003) have studied the overall effect of dose rate on X-ray diffraction intensities by monitoring changes in $R_{\rm merge}$ and diffracted intensities relative to the first image for three different samples. They concluded that for flux densities up to 10^{15} photons s^{-1} mm^{-2}, radiation damage at the macroscopic level is proportional to the total dose and is not dependent on the X-ray dose rate. In contrast, Ravelli *et al.* (2002) found a dose-rate-dependent increase in unit-cell parameters for holoferritin. It was suggested that this might have arisen from sample heating by absorption in the iron core. Another study (Leiros *et al.*, 2001) indicated that both the dose rate and the total absorbed dose may play important roles in the amount of radiation damage observed.

Heating of the crystal can be a problem as free radicals can diffuse more rapidly if the crystal temperature is elevated sufficiently. Kriminski *et al.* (2003) calculated a temperature increase of 6.5 K for protein crystals in a cryogenic N_2 gas stream, indicating that a macromolecular crystal should be maintained at a temperature below that of any reported phase transition (Weik *et al.*, 2001). Our experience for the majority of experiments performed at the ESRF is that beam heating is not a major problem for most protein crystals (Ravelli *et al.*, 2002), holoferritin being a special case owing to the high concentration of iron in the protein core.

Table 1
Statistics for the dose and dose rates calculated for the various data series.

	drMTH-Rate8	drMTH-Rate37	drMTH-Rate75	BT-Rate1	BT-Rate5	BT-Rate24
Beam size (μm)		40×60			40×50	
'Before' and 'after' data sets						
Photons s^{-1}		2.9×10^{10}			2.9×10^{10}	
Absorbed dose (Gy)		3.1×10^{6}			5.9×10^{5}	
Burn						
Photons s^{-1}	3.0×10^{11}	1.5×10^{12}	2.9×10^{12}	3.9×10^{10}	2.0×10^{11}	9.5×10^{11}
Total exposure time (s)	120	24	12	483	96.6	20
Absorbed dose (Gy)		$5.7\ (\pm 0.1) \times 10^{6}$			$3.8\ (\pm 0.1) \times 10^{6}$	
Relative dose rate	8	37	75	1	5	24

The Henderson limit indicates the absorbed dose a crystal can withstand before losing half of its original diffractive intensity and is estimated to be 2×10^7 Gy (1 Gy = 1 J kg^{-1}; Henderson, 1990). The program *RADDOSE* (Murray *et al.*, 2004, 2005) provides an easy tool to estimate for any crystal the absorbed dose and the time before the Henderson limit is reached. Important parameters in this calculation are the X-ray intensity and shape of the incident beam and the X-ray absorption coefficient of the sample; the latter is calculated based on the atomic composition of both the solvent and the protein. The effective lifetime is reduced when data collection is undertaken close to an absorption edge, since here the photoelectric cross-sections are greatly elevated for some atoms.

Radiation damage is a problem when the conventional MAD and SAD phasing methods are used (Ravelli *et al.*, 2005; Rice *et al.*, 2000) since radiation damage introduces an overall non-isomorphism within the data set. Specific structural damage including loss of definition for the anomalous scatterers also occurs (Banumathi *et al.*, 2004; Zwart *et al.*, 2004). In some cases, radiation damage has been used both to solve the phase problem of macromolecular structures (Banumathi *et al.*, 2004; Ravelli *et al.*, 2003; Schiltz *et al.*, 2004; Zwart *et al.*, 2004) and to gain more detailed information about the catalytic mechanism of enzymes (Adam *et al.*, 2004; Berglund *et al.*, 2002). However, when the aim of the data collection is to obtain SAD or MAD phasing information from anomalous scatterers it is obviously important not to lose the signal from these atoms. Therefore, knowledge about how these heavy atoms behave in the most intense X-ray beams is important.

This study systemically investigates the effect of X-ray dose rate on the radiation-damage-induced structural changes. The investigation focuses on the specific changes observed for two proteins when different dose rates but the same total absorbed dose are applied to induce radiation damage. Our results show a small but significant dose-rate dependence in the amount of specific structural changes at different dose rates, where the lowest dose rate used gave less specific damage.

2. Experimental procedures

2.1. Crystallization, data collection and processing

Two complementary samples were used in this investigation. The 67 kDa selenomethionine-substituted maltooligosyltrehalose trehalohydrolase from *Deinococcus radiodurans* (drMTH) was prepared as described by Timmins *et al.* (2005). DrMTH contains 602 residues, of which seven are selenomethionine (SeMet) residues and two are cysteine residues. Cys127 is a free cysteine, whereas Cys395 forms a disulfide linkage with a β-mercaptoethanol (Bme) molecule. The crystals were grown by the hanging-drop method and the reservoir solution contained 20% PEG 2000 MME, 0.1 *M* Tris–HCl pH 8.5, 5% glycerol and 0.1 *M* $MgCl_2$. The 4 μl drops consisted of a 1:1 mixture of protein (6 mg ml^{-1}) and reservoir solution. The drMTH crystals were cryoprotected in a solution containing 20% trehalose, 25% PEG 2000 MME, 0.1 *M* Tris–HCl pH 8.5 and 0.2 *M* $MgCl_2$ and were flash-cooled at 100 K in a cryostream. DrMTH crystals tend to be rather small, with sizes around $100 \times 30 \times 10$ μm, making translation and collection of multiple data sets from one crystal problematic. Therefore, three different crystals of similar size from the same crystallization drop were used.

The second protein studied was bovine trypsin (BT), which is a monomeric 23.5 kDa enzyme with six disulfide bridges and one calcium ion. Crystals of BT were grown by the hanging-drop method with reservoir solutions containing 25% PEG 8000, 0.2 *M* ammonium sulfate and 0.1 *M* Tris–HCl pH 8.0 (Leiros *et al.*, 2001). The 10 μl drops consisted of a 1:1 mixture of protein (15 mg ml^{-1} BT in 100 m*M* benzamidine) and reservoir solution. The BT crystal used in the study was cryoprotected in a solution comprising 15% glycerol, 25% PEG 8000, 0.2 *M* ammonium sulfate and 0.1 *M* Tris–HCl pH 8.0 and was flash-cooled in a cryostream. The BT crystal employed had dimensions of about $450 \times 50 \times 50$ μm and three different data-collection series could be collected from this one crystal.

All data were collected at ID29 at the European Synchrotron Radiation Facility (ESRF), Grenoble, France at 12.6 keV (λ = 0.984 Å) at the low-energy side of the Se *K* absorption edge. The incident photon flux was determined after calibrating the ID29 beamline diodes against a reference photodiode with known photon-flux characteristics (Ravelli & McSweeney, 2000). After the diffraction pattern had been indexed, the program *STRATEGY* (Ravelli *et al.*, 1997) was used to determine a data-collection protocol which achieved better than 98% completeness. The data-collection procedure was to collect a data set, expose the crystal to a higher dose and dose rate (a 'burn') and then to collect another data set whilst employing an identical strategy to that used for the first

Table 2
Data-collection and refinement statistics for the drMTH data series.

The space group is $P2_12_12_1$. Three different crystals were used, one for each dose-rate series. Values in parentheses are for the highest resolution bin.

	drMTH-Rate8		drMTH-Rate37		drMTH-Rate75	
	'Before'	'After'	'Before'	'After'	'Before'	'After'
X-ray statistics						
PDB code	2bxy	2bxz	2by0	2by1	2by2	2by3
Unit-cell parameters (Å)						
a	59.42	59.62	59.51	59.61	59.41	59.51
b	66.53	66.79	66.65	66.74	66.58	66.65
c	152.52	152.88	153.10	153.54	152.73	153.00
Unit-cell volume increase (%)		+0.97		+0.59		+0.45
Resolution (Å)	30–1.75 (1.84–1.75)	30–1.75 (1.84–1.75)	30–1.55 (1.63–1.55)	30–1.55 (1.63–1.55)	30–1.50 (1.58–1.50)	30–1.50 (1.58–1.50)
Mean mosaicity (°)	0.391	0.376 [−4%]	0.279	0.284 [+2%]	0.181	0.227 [+25%]
R_{sym} (%)	10.3 (44.8)	9.6 (45.9)	6.7 (26.5)	9.1 (61.8)	7.9 (37.8)	11.5 (108.6)
Max. resolution (Å) with R_{sym} of <20%	1.96	1.96	1.63	1.91	1.68	1.94
Mean $\langle I\rangle/\langle\sigma(I)\rangle$	10.4 (2.3)	10.8 (2.1)	14.5 (3.9)	11.4 (1.7)	13.0 (3.1)	9.5 (1.0)
Multiplicity	3.5 (3.5)	3.5 (3.5)	3.9 (3.8)	3.9 (3.8)	4.0 (4.0)	3.9 (3.9)
Completeness (%)	99.6 (99.2)	99.6 (99.6)	99.9 (99.8)	99.9 (99.9)	100.0 (100.0)	100.0 (100.0)
No. of unique reflections	61545	62111	89095	89654	97798	98176
Wilson *B* factor (Å^2)	12.6	14.1 [+13%]	11.5	13.4 [+17%]	10.7	14.0 [+31%]
Refinement statistics						
R factor	14.7	14.9	14.5	15.8	14.8	16.7
R_{free} (%)	18.8	18.8	17.5	19.1	17.7	20.5
R.m.s.d. bond lengths (Å)	0.017	0.017	0.016	0.020	0.015	0.021
R.m.s.d. bond angles (°)	1.465	1.474	1.600	1.739	1.645	1.792
Overall *B* factor (Å^2)	13.6	15.6 [+15%]	12.6	15.4 [+22%]	12.2	16.6 [+36%]

Table 3
Data-collection and refinement statistics for the bovine trypsin (BT) data series.

The space group is $P2_12_12_1$. Only one crystal was used for all three dose-rate series. Values in parentheses are for the highest resolution bin.

	BT-Rate1		BT-Rate5		BT-Rate24	
	'Before'	'After'	'Before'	'After'	'Before'	'After'
X-ray statistics						
PDB code	2by5	2by6	2by7	2by8	2by9	2bya
Unit-cell parameters (Å)						
a	54.26	54.26	54.22	54.23	54.25	54.27
b	58.34	58.36	58.33	58.35	58.32	58.36
c	566.75	66.76	66.75	66.77	66.73	66.78
Unit-cell volume increase (%)		+0.05		+0.08		+0.18
Resolution (Å)	20–1.30 (1.37–1.30)	20–1.30 (1.37–1.30)	20–1.30 (1.37–1.30)	20–1.30 (1.37–1.30)	20–1.30 (1.37–1.30)	20–1.30 (1.37–1.30)
Mean mosaicity (°)	0.411	0.419 [+2%]	0.426	0.436 [+2%]	0.445	0.451 [+1%]
R_{sym} (%)	6.2 (21.8)	6.4 (25.0)	7.1 (24.9)	7.1 (21.5)	6.5 (22.7)	6.8 (28.0)
Max. resolution (Å) with R_{sym} of <20%	1.30	1.37	1.45	1.45	1.37	1.45
Mean $\langle I\rangle/\langle\sigma(I)\rangle$	12.2 (4.0)	11.8 (3.6)	10.7 (3.3)	10.6 (3.0)	11.5 (3.6)	10.9 (3.1)
Multiplicity	3.8 (2.8)	3.8 (2.9)	3.7 (2.8)	3.7 (2.8)	3.7 (2.8)	3.8 (2.8)
Completeness (%)	98.9 (98.8)	98.8 (93.4)	98.7 (92.8)	98.8 (93.2)	98.8 (93.0)	98.8 (93.1)
No. of unique reflections	52088	52145	52037	52094	52043	52141
Wilson *B* factor (Å^2)	7.67	7.88 [+2.7%]	7.71	8.25 [+7.0%]	7.69	8.25 [+7.3%]
Refinement statistics						
R factor	10.3	10.4	10.4	10.8	10.3	10.8
R_{free} (%)	13.8	13.9	14.4	14.4	13.9	14.2
R.m.s.d. bond lengths (Å)	0.018	0.019	0.018	0.019	0.018	0.019
R.m.s.d. bond angles (°)	2.431	2.433	2.454	2.445	2.439	2.459
Overall *B* factor (Å^2)	7.22	7.47 [+3.5%]	7.43	8.01 [+7.8%]	7.39	7.96 [+7.7%]

data set. Hereafter, the first data set in each series is referred to as the 'before' data set, indicating it was collected before the burn. For obvious reasons the second data set is the 'after' data set. The 'before' data sets were collected with a highly attenuated beam (approximately 1% transmission) and during the X-ray burns the crystals were rotated around the same angular range as used for the 'before' and 'after' data sets. For drMTH the 'before' and 'after' data sets were collected with an oscillation range of 0.3°, three passes and 2 s exposure per frame for a total of 100°. The BT 'before' and 'after' data were collected with 1° oscillation, one pass and 1 s exposure time per frame for a total of 100° and the crystal was translated 120 µm between each series. For all crystals the data sets were collected consecutively and as fast as possible. Before any

collection or burn was started, the X-ray beam attenuation was adjusted to provide the dose rates given in Table 1.

All data were indexed and integrated using *MOSFLM* (Leslie, 1992), scaled with *SCALA* and structure factors were obtained using *TRUNCATE* (Collaborative Computational Project, Number 4, 1994). The Wilson *B* factors for each data set were calculated from 4 Å to the maximum recorded resolution. Further details are given in Tables 2 and 3. All 'before' structures were refined using *REFMAC*5 (Murshudov *et al.*, 1999) starting with rigid-body refinement of the PDB files 2bhu (drMTH) or 1hj9 (BT) and subsequent iterations of positional refinement in *REFMAC*5 (Murshudov *et al.*, 1999) interspersed with manual model building using *O* (Jones *et al.*, 1991). The 'after' models were obtained by refining the 'before' models for ten cycles of restrained positional refinement against the 'after' data sets. No attempt was made to model (manually) any radiation-damage-induced alternative conformations. For drMTH-Rate75 an attempt was made to estimate the reduction in occupancy for the Se atoms in the 'after' data by manual adjustment of the atomic occupancies and examination of difference electron-density maps. Tables 2 and 3 give the refinement statistics for all models.

2.2. Dose calculations and radiation-damage quantification

The absorbed X-ray doses were estimated using the program *RADDOSE* (Murray *et al.*, 2004, 2005) based on the crystal and X-ray beam size and shape, the photon flux, the photon energy and the crystal absorption and density, which were calculated from the unit-cell contents and the known crystallization conditions. The three drMTH crystals did not have exactly the same crystal size. However, as shown by Murray *et al.* (2005), the absorbed dose is weakly dependent on the crystal thickness and crystal size for a uniform beam. The absorbed dose is expressed as absorbed energy per mass unit; thus, small changes in crystal size give proportional changes in absorbed energy as well as total mass. For the drMTH series the photon flux is the dominant factor in the absorbed dose calculation: we estimated (using *RADDOSE*) that if the drMTH crystal volume is doubled, the error in the calculated absorbed dose is only 1.5%. For the BT series the errors are even smaller since the same nicely formed rod crystal was used for all series.

Vector difference maps $w_bF_b\exp(i\varphi_b) - w_aF_a\exp(i\varphi_a)$ were calculated to visualize specific radiation damage, taking into account the σ_A weights w (Read, 1986), the measured structure factors F and the model phases φ for the 'before' (b) and 'after' (a) data set (Ravelli & McSweeney, 2000). The peak heights (in standard deviations) in these maps were compared for the dose-rate series using peaks larger than 4σ and the relative increase in atomic B factors $[(B_{after} - B_{before})/B_{before}$; Ravelli & McSweeney, 2000; Weik *et al.*, 2000] for the most radiation-sensitive atoms was monitored.

In order to better quantify the possible loss in occupancy of X-ray-susceptible atoms, we also calculated $F_{obs} - F_{calc}$ omit maps after assigning the occupancies of the S and Se atoms to zero, followed by an additional round of refinement (ten cycles in *REFMAC*5) for the 'before' models. The 'after' structures were also refined starting from the appropriate 'before' structures. The omit maps were calculated for all six 'before' and six 'after' models. In the resulting σ_A-weighted omit maps, we integrated the spherical electron density for a radius of 1.1 Å around each Se atom and 1.0 Å around each S atoms in all the 'before' and all the 'after' structures by use of the program *MAPMAN* (Kleywegt & Jones, 1996). The relative decrease in integrated electron density (ρ) $[(\rho_{before} - \rho_{after})/\rho_{before}]$ around these atoms was subsequently calculated.

3. Results

3.1. Macroscopic changes

The changes observed in unit-cell parameters and sample mosaicity may be taken to be representative of the changes induced in the crystalline structure as a whole. The picture that emerges from consideration of the data presented in Tables 2 and 3 shows no clear indication of a dose-rate effect. The unit-cell parameters for BT (Table 3) show no significant variation arising from any of the different dose-rate burns. For drMTH (Table 2), the largest variation in unit-cell parameters is observed for the lowest dose rate used for this sample (drMTH-Rate8). In contrast, the largest change in mosaicity following a burn is observed following the drMTH-Rate75

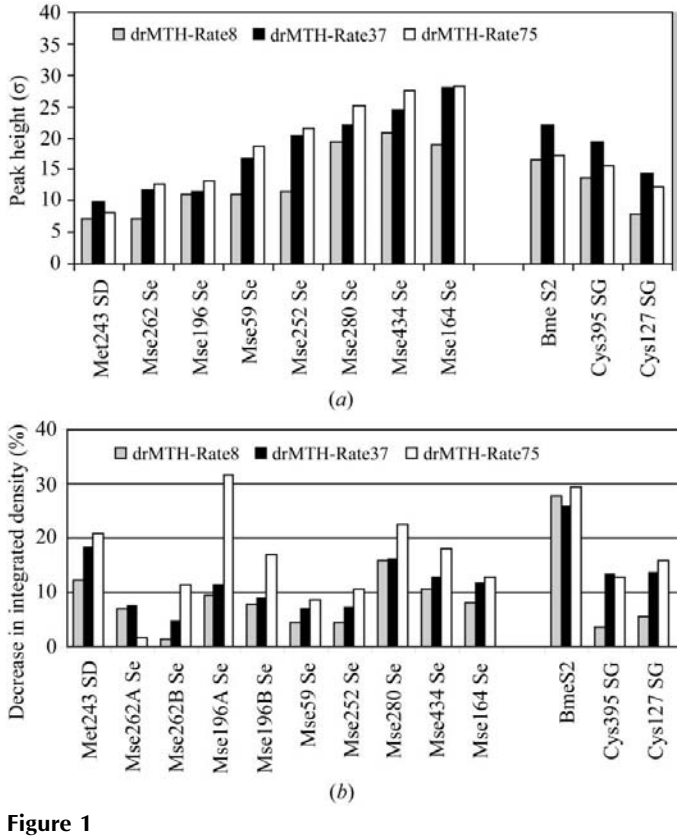

Figure 1
(*a*) Peak heights in the vector difference maps for the Se, SD, SG and S2 (in Bme) atoms of drMTH for the three dose-rate burns. (*b*) The relative decrease in integrated electron density for the three dose-rate burns as determined from σ_A-weighted omit maps.

burn, where a change of 25% is measured. No significant alteration in the sample mosaicity was observed for any of the BT experiments.

In order to estimate the changes in diffractive power of the samples, we consider the change in resolution where $R_{\rm sym}$ is greater than 20%. For drMTH, the changes induced by both the drMTH-Rate37 and drMTH-Rate75 burns are substantial. We observe a decrease in the effective resolution achievable of more than 0.25 Å. The more robust BT sample shows little loss of diffractive power at any of the burns.

The final measure of the macroscopic crystal quality considered is the Wilson *B* factor; for both samples we observe a correlation between the dose rate of a burn and the change in Wilson *B* factor.

Overall, the effect of dose rate on the macroscopic crystal properties does not provide a clear indication either for or against the presence of a dose-rate effect in our data. This observation is in accord with other investigations (Sliz *et al.*, 2003)

3.2. Selenomethionine and cysteine

For drMTH, it is clear that the most radiation-sensitive atoms are the seven Se atoms. All have high positive peaks in the vector difference maps and in terms of peak height they are all found amongst the top nine (drMTH-Rate75) and top 12 (drMTH-Rate37) and six of the Se atoms are among the top nine peaks for drMTH-Rate8. For the drMTH-Rate75 burn the peak heights are higher when compared with the drMTH-Rate37 and drMTH-Rate8 burns (Fig. 1), an indication of more radiation damage being inflicted at the highest dose rates. There is also some damage to residue 243 (Fig. 1), which has been refined as a Met residue owing to low incorporation of SeMet (Timmins *et al.*, 2005). The free cysteine residue Cys127 and the disulfide bond from Cys395 SG to Bme S2 (Figs. 1*a* and 2*a*) are most sensitive in the drMTH-Rate37 burn and less affected in the drMTH-Rate8 burn. The relative increase in atomic *B* factors, which reveals the increase in disorder following a burn, is largest for the drMTH-Rate75 burn. To gain a qualitative insight into the effective loss of order, an estimate of the Se occupancy for the 'after' drMTH-Rate75 data was made by adjusting the Se occupancies so that following *REFMAC*5 refinement no negative electron density was observable in the Fourier difference maps. In total, we estimated that about 18% of the Se-atom occupancy was lost in this data set compared with the 'before' drMTH-Rate75 data. The decrease in integrated electron density for the Se atoms (Fig. 1*b*) is largest for the drMTH-Rate75 data.

For BT, the most radiosensitive residues are the 12 cysteines, which form six disulfide bonds. The Cys220–Cys191 bridge has previously been shown to be the most sensitive (Leiros *et al.*, 2001; Ravelli *et al.*, 2003). In this experiment, Cys220 is the most radiation-sensitive residue in all three X-ray burns (Fig. 3) and the 12 Cys SG atoms are all at the top of the vector difference peak lists in the three dose-rate burns. Negative peaks close to the Cys residues indicate new relatively stable conformations appearing in the 'after' data sets (Fig. 3). The lowest dose-rate burn produces the lowest peak heights in the vector difference maps and the least decrease in integrated electron density and also the lowest increase in atomic *B* factors.

3.3. Other sensitive residues

The most sensitive residues in drMTH following the seleniums on the peak list are Asp212 and Tyr177. These residues are situated at the bottom of the drMTH active site; Asp212 OD2 is hydrogen bonded to both Tyr177 OH (2.58 Å) and water molecule W99 (2.75 Å). The catalytic active residues Glu308 and Asp400 are most altered in the drMTH-Rate37 and drMTH-Rate75 burns, with peak heights of 9.0σ (drMTH-Rate37) and 7.8σ (drMTH-Rate75) for Glu308 OE2 and 6.5σ (drMTH-Rate37) and 6.0σ (drMTH-Rate75) for Asp400 OD2 (Fig. 4; Table 4).

In these BT crystals the inhibitor benzamidine fills the active-site pocket (Fig. 5). The most sensitive residue in this region for the BT-Rate24 burn is the Ser190 OG atom (Table 5), followed by the two water molecules W18 and W27, Ser190 O and the carboxyl group of Asp189. Comparing the damage from the three different X-ray burns, BT-Rate24 has the highest peaks in the vector difference map (excepting Bza N1 and W18) when compared with the BT-Rate1 burn. For some atoms BT-Rate5 gives the most damage, but overall the lowest dose rate gives the least damage.

In drMTH there are many sensitive acidic residues found at the surface of the molecule with highly water-accessible surface area, which all have a high degree of decarboxylation. There are also many OH groups of tyrosine residues which have lost some definition, as observed by others (Burmeister, 2000). For drMTH, the tyrosine residues at positions 130, 143, 186, 189, 345 and 346 showed reduced density in the drMTH-Rate75 burn only.

4. Discussion

4.1. Is there a dose-rate effect?

At the macroscopic level, parameters such as the diffraction power of the sample, the high-resolution limit of diffraction, the sample mosaicity for the various data sets and the crystallographic unit-cell expansion (Table 2 and 3) indicate that no clear dose-rate effect is observed. This observation is consistent with previously published data (Sliz *et al.*, 2003).

At the atomic level the tendency is different: we observe that the lowest dose-rate burns (drMTH-Rate8, BT-Rate1) create less specific radiation damage in the samples. All the now 'classical' signs of X-ray radiation-induced structural changes (Burmeister, 2000; Ravelli & McSweeney, 2000; Ravelli *et al.*, 2002; Weik *et al.*, 2000, 2002) are observed to be of greater magnitude when higher dose rates are applied. Therefore, we conclude that dose-rate-related radiation damage is observable, particularly for the most sensitive atoms in the structures.

A possible cause of the features we observe is that substantial variations in the absorbed dose occurred for each

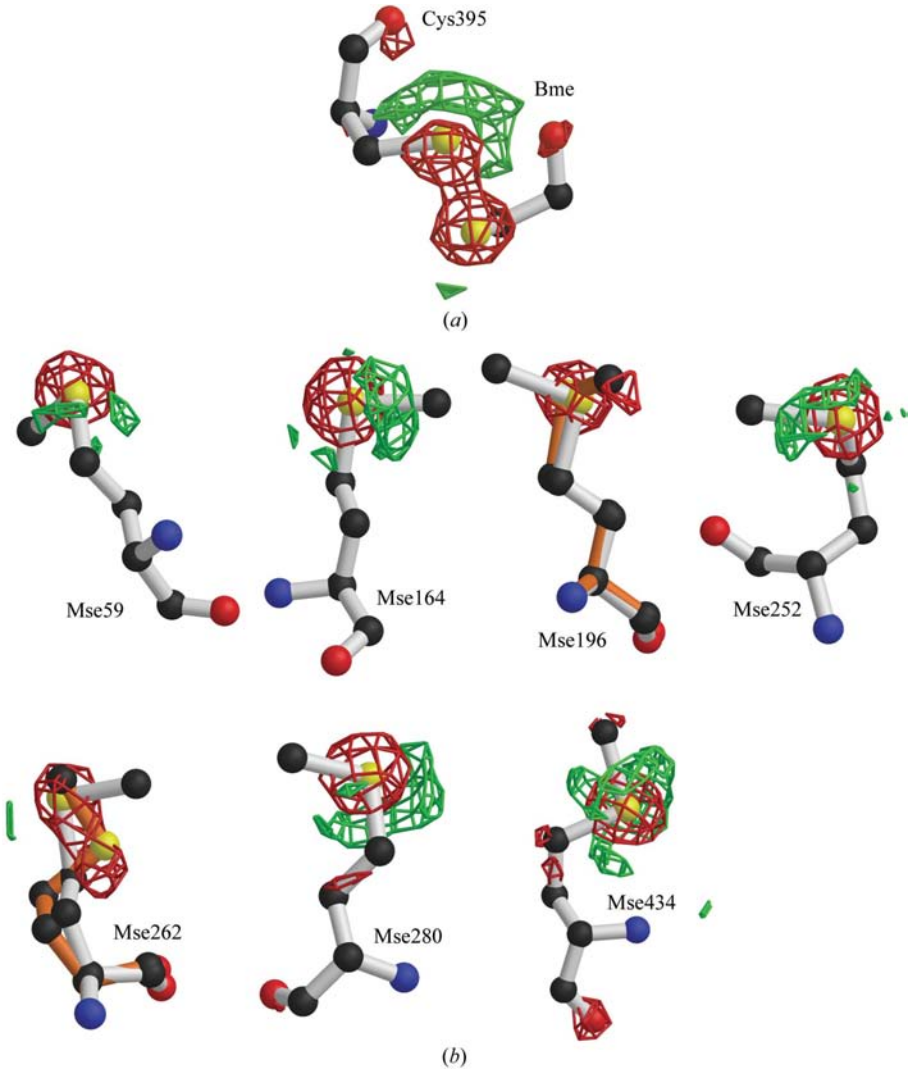

Figure 2
(*a*) Illustrations of the disulfide bond from Cys395 to the Bme residue and (*b*) the seven SeMet residues (Mse), with the corresponding vector difference map from the drMTH-Rate75 burn displayed at +4σ (red) and −4σ (green).

of these data sets. We have ruled out this possibility for a number of reasons: calibration of the X-ray beam monitors leads us to be confident that the incident flux for each data series was consistent; beam shape and size had been monitored to ensure uniform illumination of the sample; careful application of the program *RADDOSE* allows a good estimation of the absorbed dose per sample (and data collection); accurate goniometry ensures that the sample remains precisely aligned in the X-ray beam throughout data collection; previous experiments (data not shown) reproduced the results presented here.

The observed dose-rate effect appears to cause a much smaller structural perturbation than the effect of the total absorbed dose: we have observed previously that radiation damage at cryo-temperatures is mainly a function of the total X-ray dose (Ravelli & McSweeney, 2000; Weik *et al.*, 2000). The dose-rate effect we observe is thus not the major problem at the dose rate currently obtainable at third-generation X-ray sources and other experimental issues are probably of more concern. These issues include the precision of the X-ray shutter, low- and high-frequency vibrations in the beam, wobble of the spindle axis and spindle angular velocity speed variations, vibrations in the sample owing to the cryocooling system and the read-out noise of the detector. All of these issues could lead to significant errors in the data collected. However, with the increasing use of

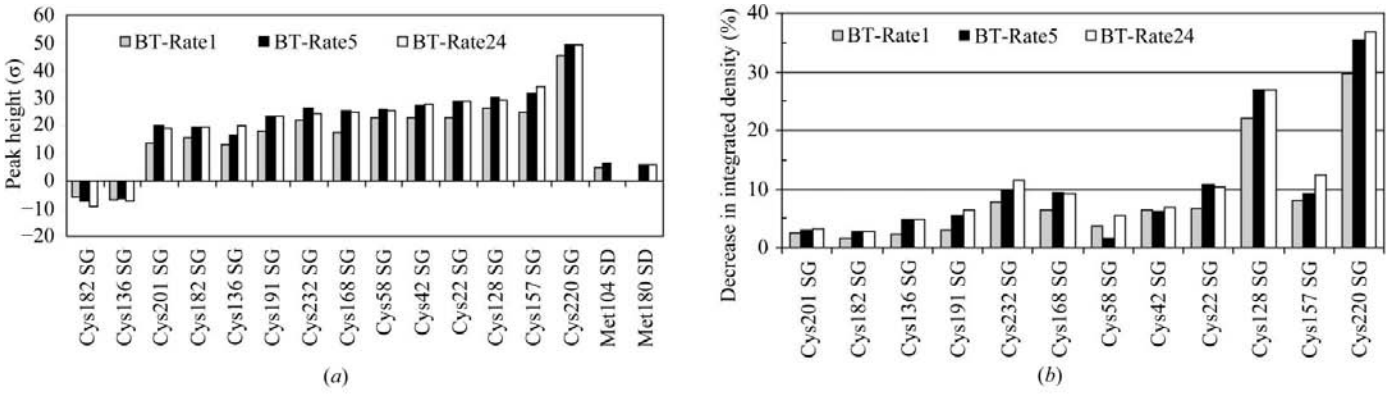

Figure 3
(*a*) Peak heights in the vector difference maps for the S atoms in cysteine and methionine residues of bovine trypsin. The negative peak heights for some Cys residues (in vector difference maps) indicate stable conformations in the 'after' data sets. (*b*) The decrease (%) in integrated electron density for the Cys SG atoms.

Table 4
Peak heights from the different dose-rate burns for the active-site residues of drMTH.

	drMTH-Rate8	drMTH-Rate37	drMTH-Rate75
Glu131 OE1	5.6	9.3	5.8
Arg273 NH2	6.2		6.5
Asp275 OD1		7.4	7.1
Asp275 OD2	5.5	5.8	5.8
W99	8.8	9.2	8.3
Arg273 NH1	7.5	7.6	9.3
Glu131 OE2	6.5	12.2	9.3
Tyr177 OH	10.0	9.7	10.2
Asp212 OD1	9.0	12.6	10.9
Asp212 OD2	10.9	11.0	12.3
Mse164 Se	18.9	28.1	28.4
Glu308 OE2	5.6	9.0	7.8
Asp400 OD1			8.2
Asp400 OD2		6.5	6.0

Table 5
Peak height in the vector difference maps resulting from the different dose-rate burns for the active site of BT.

	BT-Rate1	BT-Rate5	BT-Rate24
Asp189 OD1	4.2	7.2	7.3
Ser190 O	6.0	6.9	7.9
Ser190 OG	5.6	6.8	9.8
Ser190 CB	4.1	4.7	5.8
Tyr228 OH		5.4	5.4
Bza N2	6.1	7.7	6.8
Bza N1	6.0	5.0	5.2
W18	8.5	8.9	8.2
W27	5.0	8.5	8.6
W27	−4.1	−4.6	−4.4
W28	4.3	7.7	7.0

microfocused (and soon sub-micrometre-focused) X-ray beams for macromolecular crystallography combined with smaller sample volumes, it is possible that the dose-rate effect will become more important in the future and it is likely that sample heating would then be an important additional contributory factor.

Our experiments were undertaken at the low-energy side of the Se *K* absorption edge (drMTH) or very remote from any appropriate absorption edges (BT). If the decrease in occupancy of anomalous scatterers that we have observed is generally applicable, increased care in data collection and data treatment would be appropriate. Both the total absorbed dose and the dose rate must be chosen carefully to maximize the probability of phasing a new structure from the radiosensitive anomalous signal (Ravelli *et al.*, 2005; Rice *et al.*, 2000).

4.2. Why would a dose-rate effect exist?

This question is not a simple one to answer, but one possible explanation may be related to the steady-state free-radical concentration (including electrons) generated upon X-ray exposure. The formation, recombination and diffusion of free

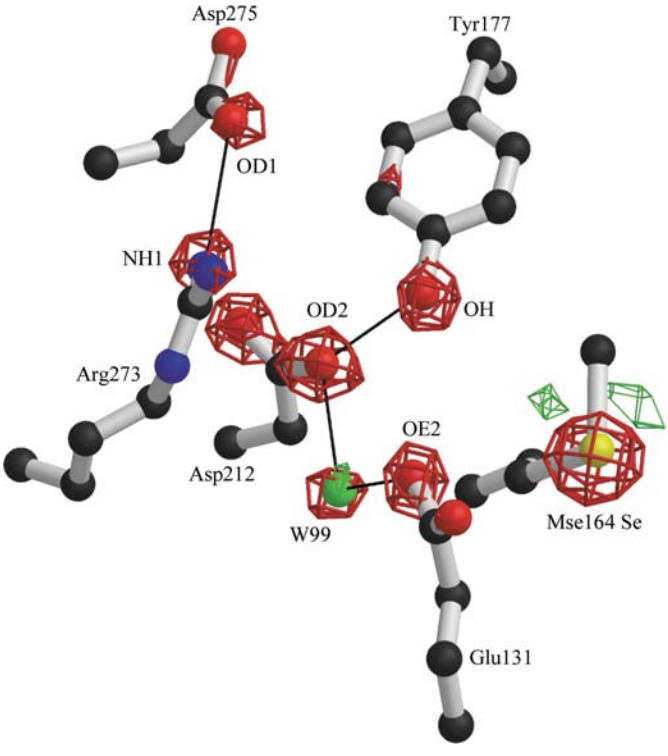

Figure 4
Active-site residues of drMTH: the vector difference map from the drMTH-Rate75 burn (+4σ is red, −4σ is green) for the sensitive residues Asp212, Tyr177, W99 and Glu131. The active-site residue Asp275 (which performs the nucleophile attack on the substrate) along with Arg273 and Mse164 are also shown.

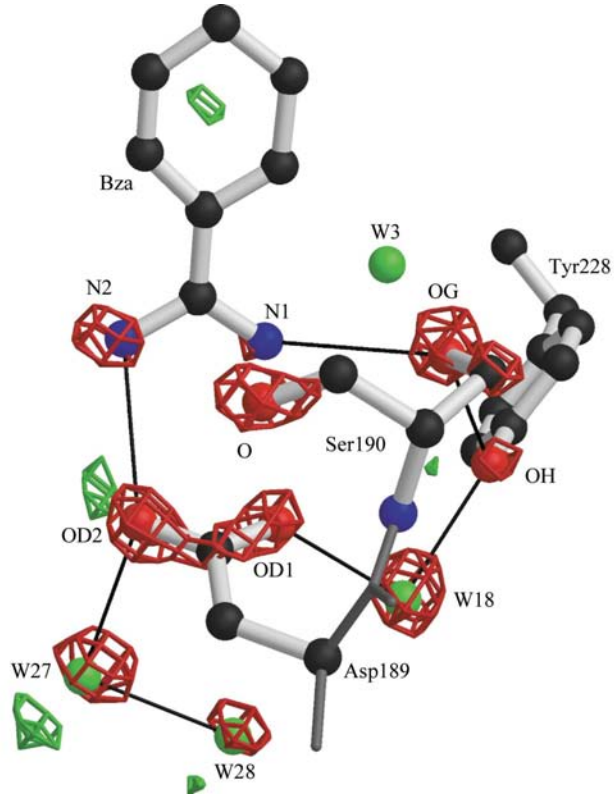

Figure 5
Active site of BT: an illustration of the binding pocket in BT with the vector difference map from BT-Rate24 contoured at +4σ (red) and −4σ (green). The inhibitor benzamidine (Bza), Asp189, Ser190, Tyr228 and some surrounding water molecules are shown.

radicals would all contribute to the total free-radical population. At the highest dose rates, free-radical recombination may not be rapid enough to quench the free-radical population, leading to diffusion of radicals and ultimately the reduction of sensitive centres. It is interesting to note that both dose-rate and inverse dose-rate effects have been observed in the study of lipidic phases (Cherezov *et al.*, 2002), where the presence of two distinct behaviours may arise from differences in the chemistry and mobility of free radicals in the lipidic systems under investigation. As has been demonstrated on a number of occasions, the chief source of photo-reduction is mobile electrons (and electron holes), both of which possess considerable mobility at cryogenic temperatures. To explain our observations one may consider that localized imbalances in free-radical numbers combined with rapid diffusion lead to observable structural changes. Globally within the crystal, the free radical concentration is not above any (unknown) critical threshold and thus those parameters which sample the long-range ordering of the crystal system (mosaicity, cell volume *etc*.) would not be expected to be sensitive to dose rate, in agreement with our observations and those previously reported. This mechanistic suggestion remains speculative and confirmation of the hypothesis requires more sophisticated experiments.

5. Conclusions

Our results show that there is an observable dose-rate effect when collecting macromolecular crystallographic data. However, the dose-rate effect observed is a secondary problem when compared with the concomitant absorbed-dose radiation damage. Care must be taken to properly utilize third-generation synchrotron sources and radiation damage is only one of a number of experimental reasons why the X-ray dose rate must be chosen carefully.

We thank Dr Bill Shepard for providing technical data on ID29 and for assistance during data collection and the ESRF review panel for scheduling us with BAG beamtime. Dr Elspeth Garman and Dr Martin Weik are acknowledged for many stimulating discussions.

References

Adam, V., Royant, A., Nivière, V., Molina-Heredia, F. P. & Bourgeois, D. (2004). *Structure*, **12**, 1729–1740.
Banumathi, S., Zwart, P. H., Ramagopal, U. A., Dauter, M. & Dauter, Z. (2004). *Acta Cryst.* D**60**, 1085–1093.
Berglund, G. I., Carlsson, G. H., Smith, A. T., Szoke, H., Henriksen, A. & Hajdu, J. (2002). *Nature (London)*, **417**, 463–468.
Burmeister, W. P. (2000). *Acta Cryst.* D**56**, 328–341.
Cherezov, V., Riedl, K. M. & Caffrey, M. (2002). *J. Synchrotron Rad.* **9**, 333–341.
Collaborative Computational Project, Number 4 (1994). *Acta Cryst.* D**50**, 760–763.
Henderson, R. (1990). *Proc. R. Soc. London Ser. B*, **241**, 6–8.
Jones, T. A., Zou, J.-Y., Cowan, S. W. & Kjeldgaard, M. (1991). *Acta Cryst.* A**47**, 110–119.
Kleywegt, G. J. & Jones, T. A. (1996). *Acta Cryst.* D**52**, 826–828.
Kriminski, S., Kazmierczak, M. & Thorne, R. E. (2003). *Acta Cryst.* D**59**, 697–708.
Leiros, H.-K. S., McSweeney, S. M. & Smalås, A. O. (2001). *Acta Cryst.* D**57**, 488–497.
Leslie, A. G. W. (1992). *Jnt CCP4/ESF–EACBM Newsl. Protein Crystallogr.* **26**.
Murray, J. W., Garman, E. F. & Ravelli, R. B. G. (2004). *J. Appl. Cryst.* **37**, 513–522.
Murray, J. W., Rudino-Pinera, E., Owen, R. L., Grininger, M., Ravelli, R. B. & Garman, E. F. (2005). *J. Synchrotron Rad.* **12**, 268–275.
Murshudov, G. N., Vagin, A. A., Lebedev, A., Wilson, K. S. & Dodson, E. J. (1999). *Acta Cryst.* D**55**, 247–255.
Ravelli, R. B., Leiros, H-.K. S., Pan, B., Caffrey, M. & McSweeney, S. (2003). *Structure*, **11**, 217–224.
Ravelli, R. B. & McSweeney, S. M. (2000). *Structure Fold. Des.* **8**, 315–328.
Ravelli, R. B., Nanao, M., Lovering, A., White, S. & McSweeney, S. (2005). *J. Synchrotron Rad.* **12**, 276–284.
Ravelli, R. B., Sweet, R. M., Skinner, J. M., Duisenberg, A. J. M. & Kroon, J. (1997). *J. Appl. Cryst.* **30**, 551–554.
Ravelli, R. B., Theveneau, P., McSweeney, S. & Caffrey, M. (2002). *J. Synchrotron. Rad.* **9**, 355–360.
Read, R. J. (1986). *Acta Cryst.* A**42**, 140–149.
Rice, L. M., Earnest, T. N. & Brunger, A. T. (2000). *Acta Cryst.* D**56**, 1413–1420.
Schiltz, M., Dumas, P., Ennifar, E., Flensburg, C., Paciorek, W., Vonrhein, C. & Bricogne, G. (2004). *Acta Cryst.* D**60**, 1024–1031.
Sliz, P., Harrison, S. C. & Rosenbaum, G. (2003). *Structure*, **11**, 13–19.
Timmins, J., Leiros, H.-K. S., Leonard, G., Leiros, I. & McSweeney, S. (2005). *J. Mol. Biol.* **347**, 949–963.
Weik, M., Bergès, J., Raves, M. L., Gros, P., McSweeney, S., Silman, I., Sussman, J. L., Houée-Levin, C. & Ravelli, R. B. G. (2002). *J. Synchrotron Rad.* **9**, 342–346.
Weik, M., Kryger, G., Schreurs, A. M., Bouma, B., Silman, I., Sussman, J. L., Gros, P. & Kroon, J. (2001). *Acta Cryst.* D**57**, 566–573.
Weik, M., Ravelli, R. B., Kryger, G., McSweeney, S., Raves, M. L., Harel, M., Gros, P., Silman, I., Kroon, J. & Sussman, J. L. (2000). *Proc. Natl Acad. Sci. USA*, **97**, 623–628.
Zwart, P. H., Banumathi, S., Dauter, M. & Dauter, Z. (2004). *Acta Cryst.* D**60**, 1958–1963.